Forcing Space: An Alternative to Regime Diagrams for Predicting Characteristics of Turbulence in the Ocean Surface Mixing Layer

ANN E. GARGETT[a,b]

[a] *Institute of Ocean Sciences, Sidney, British Columbia, Canada*
[b] *Old Dominion University, Norfolk, Virginia*

(Manuscript received 8 July 2021, in final form 29 December 2021)

ABSTRACT: Various forms of regime diagrams have become an accepted means of identifying the dominant type of forcing of turbulence in the ocean surface layer. However, all of the proposed forms share a number of issues, demonstrated here, that make them an imperfect tool for this purpose. Instead, I suggest a forcing space consisting of surface buoyancy flux (usually dominated by surface heat flux) and a growth rate defined as the inverse of a theoretical time scale for growth of Langmuir circulations in an unstratified water column. Using coastal data, it is demonstrated that, provided forcing conditions are roughly constant for several hours, location in the upper half-plane of this forcing space predicts organizational characteristics of observed turbulence that range in a systematic way between those of "pure" convection and those of full depth Langmuir circulations. In this upper half-plane, where a convective scale velocity exists and the surface Stokes drift velocity can be computed, allowing calculation of a Stokes scale velocity, a linear combination of the two scale velocities provides a consistent estimate of observed rms turbulent vertical velocity. Time dependence is nevertheless a frequent characteristic of ocean surface layer forcing, if only because of the (usually large) diurnal variation in surface heat flux. It is shown that the time scale of response of surface layer turbulence to time variable forcing depends on whether the major change is due to wind/wave or buoyancy forcing. Relevant modeling studies are suggested.

KEYWORDS: Atmosphere-ocean interaction; Langmuir circulation; Oceanic mixed layer

1. Introduction

The influence of surface waves on generation of turbulence in marine surface boundary layers is profoundly asymmetric between the atmosphere and the ocean. In the atmospheric boundary layer (ABL), the effect of surface waves is predominantly to modify the surface roughness perceived by the atmosphere. However, on the ocean side of the air–sea boundary, surface waves, through the shear of their Stokes drift velocity (Craik and Leibovich 1976), are a singular and often powerful source of turbulence in addition to the sources (mean shear and destabilizing buoyancy flux) common with the ABL.

Turbulence in the upper-ocean boundary layer has increasingly been analyzed in terms of regime diagrams, pioneered by Li et al. (2004). Regime diagrams are spaces of two nondimensional numbers derived by scaling either the turbulent momentum equation (Li et al. 2004; Gargett and Grosch 2014, hereinafter GG14) or the turbulent kinetic energy equation (Belcher et al. 2012). All three derivations scale velocity with the (water-side) surface stress velocity $u_* = \sqrt{\tau/\rho_w}$ (where τ is surface wind stress and ρ_w a characteristic mean seawater density), while the second scale parameter varies among authors. Li et al. (2004) use a length scale associated with the *e*-folding depth of the wave field, Belcher et al. (2012) use a length scale that is simply stated to be the mixed layer depth, and GG14 use a time scale for growth of wave-forced Langmuir circulations derived theoretically by Leibovich (1977). Regardless of the underlying scalings, it is then argued that in different regions of such diagrams, generation of turbulence is dominated by mean shear, Stokes shear, or surface buoyancy (heat) transfer when this is destabilizing to the ocean. While regime diagrams have been utilized in analysis of large-eddy simulations (LES) of the upper ocean and, to a more limited extent, of ocean observations, I will argue that they are flawed for interpretation of turbulence in the real ocean surface layer (OSL) and are more usefully replaced by a "forcing space." Provided knowledge of surface forcing fields, forcing space provides prediction of the organizational character of OSL turbulence, plus a first quantitative prediction of its strength in cases of quasi-steady mixed wave and buoyancy forcings.

I will assess the usefulness of forcing space versus regime diagrams using direct and simultaneous measurements of both the surface wave field and the large eddies of OSL turbulence from an upward-looking VADCP (a standard ADCP with an additional central fifth beam) that was bottom-mounted in15-m water depth at a coastal cabled observatory (LEO) for approximately 6 months. Full descriptions of the instrument, adjustment of the fifth beam to vertical, techniques used to derive turbulence information, and details of accompanying observations of atmospheric forcing fields can be found in Gargett and Wells (2007). Processing used to derive surface wave data from fifth-beam velocities is described in the appendix of GG14. Data will be referenced by session (e.g., LEO043), a set of time-consecutive records, each ~2 h in length. Individual records within a session will be referenced by session number plus a two-digit record number (e.g., 043.05), or by record number alone if the session is clear.

Corresponding author: Ann Gargett, gargettann@gmail.com

DOI: 10.1175/JPO-D-21-0145.1

Turbulence data used are restricted to time periods when vertical velocity variance averaged over depth and record length in time exceeded a noise level of 9×10^{-5} (m s^{-1})^2 and the entire water column was unstratified, defined as exhibiting less than 0.5°C difference in temperature between the top and bottom of the water column. The latter requirement facilitates comparison with the deep-ocean mixed layer, and also automatically rejects situations where available observations would not have sufficient resolution for surface-forced turbulence confined to a shallow upper layer. Records satisfying these two conditions will be referred to as unstratified. In situations requiring a value for the surface Stokes drift velocity U_{S0}, it will also be required that the measured surface Stokes velocity spectral function (see appendix) exhibits a defined peak before 0.4 Hz, the highest accepted frequency of the measured wave displacement spectrum, so that U_{S0} can be computed (for details, see appendix). Records satisfying all three conditions will be termed "good."

I first describe issues common to all extant forms of regime diagram (section 2), then introduce forcing space and illustrate its advantages in predicting the character and relative strength of turbulent large-eddy structures when forcing conditions are relatively steady (section 3). I next introduce and assess a prediction of the magnitude of turbulent vertical velocity variance in conditions of quasi-steady mixed Stokes and buoyancy forcing, based only on knowledge of surface forcing parameters (section 4). Finally, I illustrate different time scales of adjustment of turbulence character and strength to temporal changes in buoyancy or wind/wave forcing fields (section 5).

2. Issues with regime diagrams

All three forms of regime diagram referred to above use a Langmuir number as one of two nondimensional parameters. I follow GG14 in using a Langmuir number La defined as the ratio of u_* to U_{S0}, i.e.,

$$\mathrm{La} \equiv \frac{u_*}{U_{S0}} \tag{1}$$

[although most authors follow McWilliams et al. (1997) in using $\mathrm{La}_t \equiv \mathrm{La}^{1/2}$, La_t inevitably appears squared in scaled equations so its square is the more straightforward usage]. In calculation and use of La, three issues arise.

a. Uncertainties in correction of U_{S0} calculated from surface wave frequency spectra measured up to a finite upper-frequency f_M for missing variance due to waves of higher frequencies

It is standard practice to use a measured surface wave displacement spectrum in the expression of Kenyon (1969) to derive a Stokes function whose integral over frequency is the Stokes velocity (hence use of the term function rather than spectrum by GG14). Evaluating this integral at the surface $x_3 = 0$ (x_3 defined positive upward from the surface) provides U_{S0}. However, observations provide the wave displacement spectrum only to some upper-frequency f_M (generally of order 0.5 Hz), hence must be corrected for variance missing at higher frequencies. This correction has been done in slightly different ways by different authors, but all methods depend on some model of the high-frequency form of the wind-forced surface wave displacement spectrum. Belcher et al. (2012) use the Phillips (1958) f^{-5} form for all $f > f_M$. Clarke and Van Gorder (2018, hereinafter CVG) transition from a now widely accepted Toba (1973) f^{-4} form at f_M to the Phillips form at a wave breaking frequency f_B determined by Forristall (1981), where the correction is terminated (CVG reasonably assume that waves with higher frequencies make no contribution to a first-order nonlinear Stokes velocity). A slightly modified version of the latter method (details in appendix) is used here to correct values of U_{S0} when waves are wind forced (the resulting corrections are not strongly dependent on which of the three methods are used). However, an unaddressed problem with such corrections arises if waves are *not* being actively forced by the local wind, i.e., when dominant waves are either remotely generated swell or waves that, while locally generated, are slowly decaying following a wind stress event. During such periods, which occupy a nonnegligible fraction of the time at LEO, observed spectra should not be corrected by an algorithm that assumes wind-forced waves. Since there is no proven algorithm for high-frequency extension when waves are identified as being "not wind forced" (using the ECMWF criterion, see appendix of Bidlot 2020), in these cases the value used for U_{S0} remains the value determined by integration to f_M.

Differences due to missing variance corrections can be substantial, as seen in the regime diagram of Fig. 1, the log {Ra, La} diagram of GG14, where color codes turbulent vertical velocity variance $\mathrm{wvar} \equiv \overline{\langle w'^2 \rangle}$ averaged over record length (~2 h) in time ($\langle\rangle$) and over depth (overbar). La [Eq.(1)] is the ratio of stress forcing to Stokes (Langmuir) vortex forcing in the scaled turbulent momentum equation. The ratio of buoyancy to stress forcing in this equation is a Rayleigh number

$$\mathrm{Ra} \equiv \frac{\alpha g}{k_T} Q t_*^2 = \frac{\alpha g}{k_T} \frac{Q}{g_*^2}, \tag{2}$$

where $\alpha > 0$ is the coefficient of thermal expansion and k_T the thermal conductivity of seawater, and $Q > 0$ is the heat gain of the atmosphere during convective conditions (to retain continuity with atmospheric boundary layer conventions, GG14 defined Q as the surface heat flux to the atmosphere from the ocean: thus $Q > 0$ is destabilizing to the ocean). The time scale

$$t_* \equiv \left(\frac{dU_S}{dx_3}\frac{dU}{dx_3}\right)^{-1/2} = \left[\left(\frac{dU_S}{dx_3}\right)_{x_3=-3\mathrm{m}} \frac{u_*}{H}\right]^{-1/2} \tag{3}$$

in (2) is the form used by GG14 (see their appendix) for that derived by Leibovich (1977) for growth of Langmuir circulation (LC) in an unstratified sheared fluid. Since observations include both signs of Q, the regime diagram of GG14 plots records with stabilizing flux ($Q < 0$) as $-\log(|\mathrm{Ra} < 0|)$ in the lower half-plane.

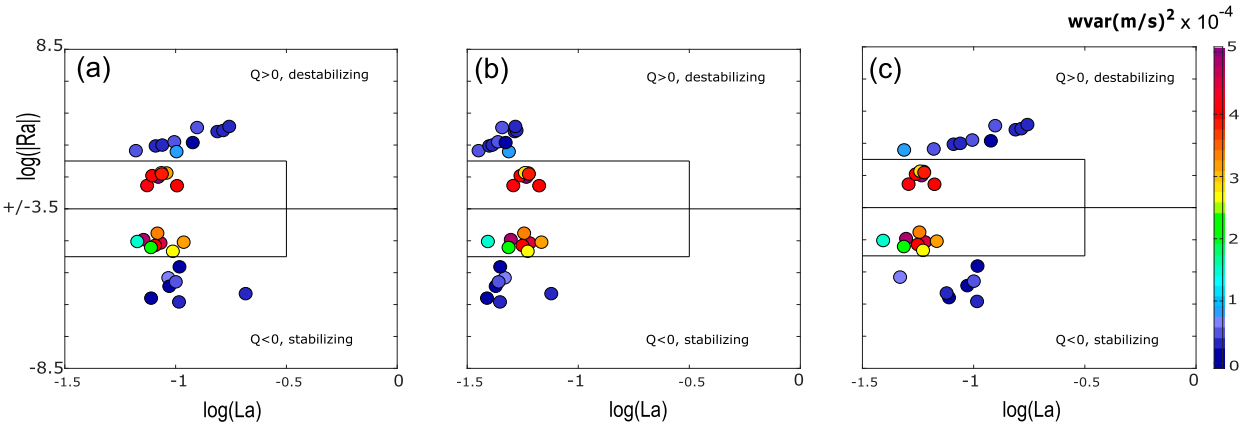

FIG. 1. Modification of the log{Ra, La} regime diagram of GG14 for LEO043 caused by various choices for computing U_{S0}. (a) U_{S0} uncorrected for variance missing at frequencies higher than $f_M = 0.4$ Hz, the maximum frequency used for measured wave displacement spectra. (b) Correction to U_{S0} (see appendix) that assumes wind-forced waves in all records. (c) The same correction for wind-forced waves, but no correction for records in which waves do not satisfy an ECMWF criterion for wind-forced waves. The boxes in the figure delineate boundaries, proposed by GG14 using uncorrected U_{S0}, that ensure the large eddies of turbulence have characteristics of full-depth Langmuir circulations. Color codes wvar $\equiv \overline{\langle w'^2 \rangle}$, the turbulent vertical velocity variance averaged over time (~2 h) of each record ($\langle\rangle$) and depth (overbar).

The regime diagram of Fig. 1a uses good data from LEO043, the iconic Langmuir supercell (LSC, defined by Gargett et al. 2004) event at LEO, before correction of wave-derived parameters [U_{S0} and $(dU_S/dx_3)_{x_3=-3\mathrm{m}}$] for missing variance. In Fig. 1b, both parameters in all records are corrected with the wind-forced wave algorithm described in the appendix, while in Fig. 1c they are corrected *only* if the wave field satisfies the ECMWF criterion for wind-forced waves. Note that although the effects of correction for missing variance on La can be considerable, there is almost no effect on Ra because Stokes shear at the depth $x_3 = -3$ m that GG14 use in evaluating (3) is essentially unaffected by the correction (see appendix).

An unrelated issue with determination of U_{S0} occurs when an observed (uncorrected) Stokes function associated with wind-forced waves does not have a defined peak within the range of frequencies measured. The value of U_{S0} is considered undeterminable in such cases, fortunately rare.

b. *In wind-forced wave conditions in the ocean, La is roughly constant*

If $U_{S0} = C_S u_*$, with C_S a constant, then the Langmuir number $\mathrm{La} = C_S^{-1}$ is constant. The earliest observational study suggesting that this is indeed the case on average in wind-forced seas was that of Belcher et al. (2012) who used ERA-Interim wave model data from the Southern Ocean (their Fig. 3) and found $\mathrm{La}_t \sim 0.3$, corresponding to $\mathrm{La} \sim 0.1$, hence $C_S \sim 10$. A large set of LEO measurements (Fig. 2), also show a relatively linear relationship between U_{S0} (corrected for missing variance) and u_*, with a value of C_S approximately the value of 12 determined by GG14 using uncorrected U_{S0} values and a smaller dataset. CVG used simultaneous wind and wave gauge measurements from a wider range of shelf and deep ocean buoys and found (their Fig. 5) $C_S \sim 7$. However, CVG applied a factor of 0.8 to their values of U_{S0} to roughly account for directional spread in the surface wave field: removing this correction gives a value of $C_S \sim 9$. Despite some variation in C_S among these datasets, consistent with minor variation in data and/or methods used in calculation of U_{S0} and/or u_*, together they provide strong evidence of a roughly linear relationship, at least in an averaged sense, between the two fields whose ratio forms La.

In the absence of surface buoyancy forcing, roughly constant $\mathrm{La} \ll 1$ has been interpreted as demonstrating dominant turbulence production by wave (Stokes) forcing over any that might be associated with a classical sheared boundary layer. In itself an important result of present regime diagrams, it

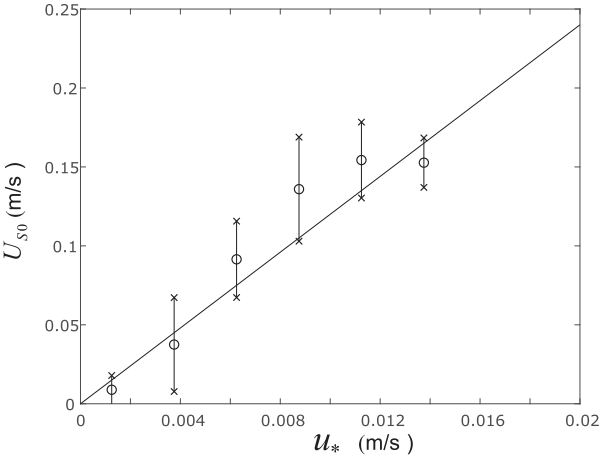

FIG. 2. Relationship between corrected surface Stokes velocity U_{S0} and surface stress velocity u_*. Values of U_{S0} determined for 266 individual records (regardless of stratification, since only surface wave properties are used) are sorted into bins of record-averaged u_* before averaging. The straight line has the slope of 12 previously determined by GG14 using a smaller dataset.

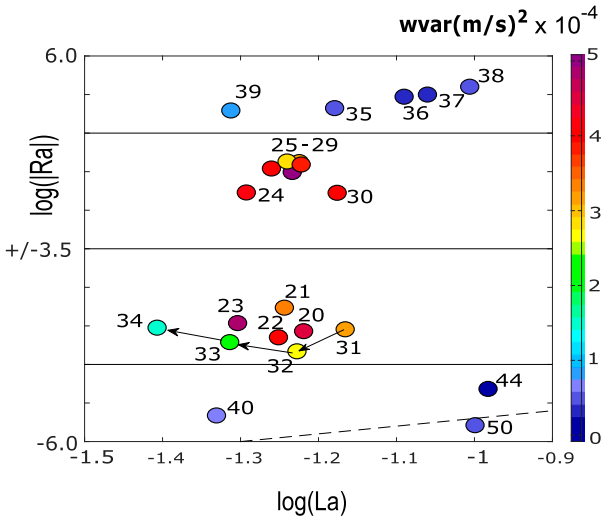

FIG. 3. Enlargement of an area of Fig. 1c, highlighting records during the supercell event that starts in record 20. Despite stabilizing heat flux at the time, records 20–23 at the height of the storm exhibit all the characteristics of full-depth LC, while records 31–34 with essentially the same Ra values later in the storm move to lower La while structures weaken. This behavior is counter to the expectation that lower La implies stronger Stokes forcing, hence stronger LC, and demonstrates that characteristics of observed turbulence depend not only on the value of La but on *how that value is achieved*.

nevertheless means that in an averaged sense, La does not provide additional information about turbulence properties. However, the conclusion that La is approximately constant is based on highly averaged data, and with individual shorter data periods there is significant scatter. Can this scatter at least be interpreted as increasing dominance of Stokes forcing, hence stronger LC, as La decreases? Unfortunately not.

c. *The expectation that smaller La is associated with stronger Stokes forcing can be shown to be unfounded*

When buoyancy forcing is weak or absent, smaller La in regime diagrams is widely associated with increased dominance of wave forcing over stress forcing (Li et al. 2004; Harcourt and D'Asaro 2008; Belcher et al. 2012; Yoshikawa et al. 2018, among others) A clear counterexample to this expectation is seen in the enlargement (Fig. 3) of a portion of the full regime diagram of Fig. 1c. Records 20–23 occur during the peak wind stress and wave amplitudes observed during the storm causing the supercell event, exhibit distinctive features of LC and large turbulent vertical velocity variance, and have surface heat gain magnitude comparable to records 31–34. However, these latter records are characterized by a continued decrease in turbulent vertical velocity variance wvar and loss of structural organization, *despite moving to progressively smaller values of* La. This behavior, at near-constant Ra, is opposite to the assumed increase in Langmuir forcing relative to mean shear forcing as La decreases. The changes observed are in fact due to rapid decrease in wind stress (starting in record 31 and nearing zero by record 35) at the end of the storm while, in contrast, wave amplitude declines much more slowly and peak wavelength hardly changes. The observed decrease in La during these records is thus *not* evidence of increasing dominance of wave forcing over shear forcing, hence strengthened LC, but is rather associated with *weakened* LC, caused by sharp decrease in u_* accompanied by more gradual decrease in U_{S0}. Simulations based on Reynolds-averaged Navier–Stokes (RANS) equations augmented with Craik–Leibovich vortex forcing are found to reproduce this behavior when the Langmuir number of the simulation is reduced by reducing the magnitude of u_* while keeping (single) wave parameters fixed (A. Tejada-Martinez 2021, personal communication).

These observations reveal a fundamental shortcoming in use of a regime parameter that, like La, involves *ratios* of scaling variables, since the value of the parameter can be achieved by different combinations of these variables. The observational data in Fig. 3 show that characteristics of the turbulence actually observed can depend not only on the value of a regime parameter, but on *how that value is achieved*.

Although the first two issues described above are unique to the Langmuir number, this final issue also afflicts the second nondimensional parameter in any of the proposed regime diagrams, since these are all some ratio of forcing parameters. Again using the regime diagram of GG14 as an example, the same value of Ra can be achieved with different combinations of Q characterizing convective forcing and time scale t_* characterizing Stokes forcing.

3. Forcing space as an alternative to regime diagrams

To provide a means of reliably determining the character—and hopefully the strength—of upper-ocean turbulence under the influence of multiple forcing mechanisms, it seemed advisable to move from the nondimensional ratios of present regime diagrams to a space of more directly interpretable forcing parameters. The first chosen parameter is surface buoyancy flux B_o, used as a measure of buoyancy forcing and computed from the (assumed dominant) surface heat flux Q as $B_o = g\alpha Q/\rho_o C_v$, where $g = 9.81$ m s^{-2} is acceleration due to gravity, $\alpha = 1.7 \times 10^{-4}$ K^{-1} is the thermal expansion coefficient of seawater at the surface layer temperature of 10°C typical of LEO, $\rho_o = 1024$ kg m^{-3} is a reference seawater density and $C_v = 4.19 \times 10^3$ J kg^{-1} K^{-1} is the specific heat of seawater at constant volume. The second parameter chosen is $g_* = t_*^{-1}$, the LC growth rate related to Leibovich's time scale t_*, used as a measure of wind/wave forcing (use of g_* rather than t_* provides a parameter with the desirably intuitive property of increasing with increasing magnitude of the underlying forcing).

The particular definition used for g_* (that introduced by GG14, using Stokes shear evaluated at a fixed depth of $x_3 = -3$ m) has the advantage of not involving any wave variable at the surface itself (in particular, Stokes shear as evaluated from measured surface wave displacement spectrum is unpleasantly infinite at $x_3 = 0$). An additional advantage of this definition is that a shear value determined

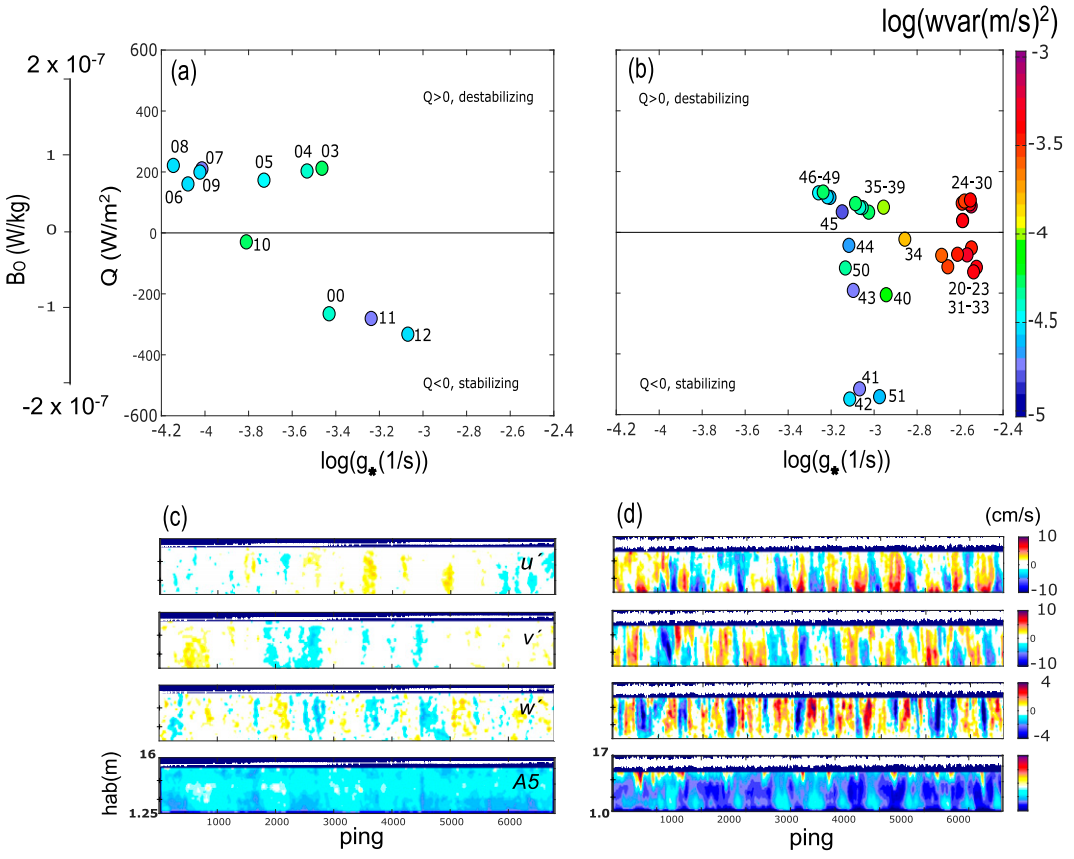

FIG. 4. Distribution in proposed forcing space of unstratified records from (a) LEO161, taken during a cold air outbreak with near-zero wind stress and a wave field consisting only of swell and (b) LEO043, the iconic storm-forced LSC event at LEO. Using the logarithm of g_* expands resolution: in the same vein, color-coding log(wvar) reveals increased detail of signal strength. Visualizations below show horizontal fluctuation velocity components in coordinates oriented along (u') and across (v') record-average wind direction, vertical fluctuation velocity w', and backscatter amplitude A5. The order of fields shown on the panels of (c) Record 161.08, the archetype for pure convection, is the same in (d) Record 043.24, the archetype for strong, well-organized LSC. Velocity scales (± 10 cm s^{-1} for u', v', ± 4 cm s^{-1} for w') are the same for both records. Backscatter is corrected for range and beam spread but uncalibrated. Backscatter scales have the same range (20 units) but differ in offset (70 for LEO161, 80 for LEO043). All fields are Hanned over three (0.4 m) range bins in the vertical and 121 (1 s) pings and displayed as functions of time (ping) and hab = height above bottom.

at this depth in the water column is almost unchanged by correction for loss of variance (see appendix), hence has none of the uncertainty associated with that process in U_{S0}. A final advantage is that this value of Stokes shear, hence g_*, can be computed for every record, unlike U_{S0} which cannot be reliably computed when waves are not wind forced and/or the measured surface Stokes function has its maximum too near f_M.

Figure 4 shows unstratified records in this forcing space[1] for two defining sessions [log(g_*) is used to expand resolution]. Color codes the logarithm of wvar, where again the logarithm is used to provide detail. LEO161 (Fig. 4a) is an unusual cold air outbreak, characterized by surface heat loss combined with very weak offshore winds, hence a swell-dominated wave field. Record 161.08 is used as archetype for "pure" convection (CVN), defined as convection in the near absence of wind waves and with minimal mean shear. LEO043 (Fig. 4b) is the well-described Langmuir supercell event (Gargett et al. 2004) in which LSC are forced by storm winds and seas: record 043.24 has been used as an archetype for LSC. The regions of forcing space occupied by the two sessions are almost completely disjoint. LSC records of LEO043 lie at high values of g_* and values of Q (of either sign) that are less than ~(100–150) W m^{-2}, while the CVN records of LEO161 have magnitudes of Q that are only slightly larger (~200 W m^{-2}),

[1] Axes for both B_o and Q are shown in forcing space plots, since these two fields will be used interchangeably in the present discussion. However, since correspondence between the two fields will differ in regions with different surface layer temperature (hence different α), B_o is the more fundamental parameter.

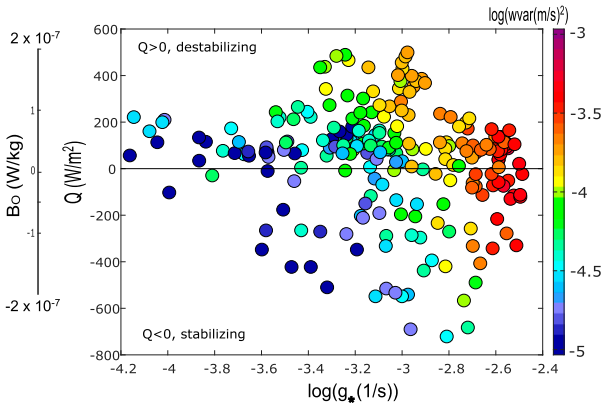

FIG. 5. Locations in forcing space of all unstratified data from LEO sessions 043, 128, 129, 154, 159, 160, 161. Color codes log(wvar).

but values of g_* that are nearly two orders of magnitude smaller.

The characteristics of turbulence associated with the CVN and LSC end-members are dramatically different, as illustrated by visualizations of turbulent velocities and backscatter. Record 043.24 (Fig. 4d) exhibits the highly organized large-eddy structures characteristic of LSC. Regions of downward fluctuation vertical velocity (w') are associated with bottom-intensified downwind fluctuation velocity (u'), and change in sign (determined by the sign of crosswind mean flow) of near-bottom crosswind fluctuation velocity (v'). Backscatter exhibits typical plumes of surface/bottom origin in downwellings/upwellings, associated with surface-origin air bubbles and bottom-origin sediment, respectively. In contrast, the CVN record 161.08 (Fig. 4c) shows random fluctuations in all three velocity components and no obvious structure in the backscatter signal. CVN is also associated with considerably weaker turbulent velocities: mean square turbulent vertical velocity $\langle \overline{w'^2} \rangle$ above noise is only 2.7×10^{-5} (m s^{-1})^2 for 161.08, compared to 3.9×10^{-4} (m s^{-1})^2 for 043.24.

While the LSC end-member is observed during any extended period of storm force winds, the CVN end-member was seen in only ~8 h (records 161.06–09) during the nearly 6 months of the LEO deployment. In Fig. 5, a compilation of unstratified records from several sessions, most records in the upper half-plane of forcing space fall between these two end-members, indicating some mix of convective and Stokes forcing. Can location in forcing space enable identification of the character and/or magnitude of expected turbulent large-eddy structures?

Structural identification of the degree of convective relative to Stokes forcings is hampered by the fact that unstable convection is organized into roll vortices by the presence of a mean shear flow (Etling and Brown 1993). Paired counterrotating vortices of sheared convection have the same features used to identify LC, change of sign of the cross flow at the top and bottom of upwellings/downwellings, and accelerated flow in the downflow direction over downwellings. It is nonetheless the case that observations in different areas of forcing space do exhibit consistent qualitative differences, as well the quasi-systematic difference in wvar that is clear in Fig. 5 and will be discussed in section 4.

To illustrate differences in character of turbulent structures in different parts of forcing space, I will use measurements from two sessions (LEO159 and LEO160) that include a wide range of forcing combinations. The two sessions, although consecutive in time, are shown separately in Fig. 6 to enable location of individual "clusters" of records.

In Fig. 6, clusters are loosely defined as groups of time-consecutive records having similar values of Q (B_o) and log(g_*), i.e., quasi-steady forcing. Figure 7 provides visualizations of turbulent velocities and acoustic backscatter for one

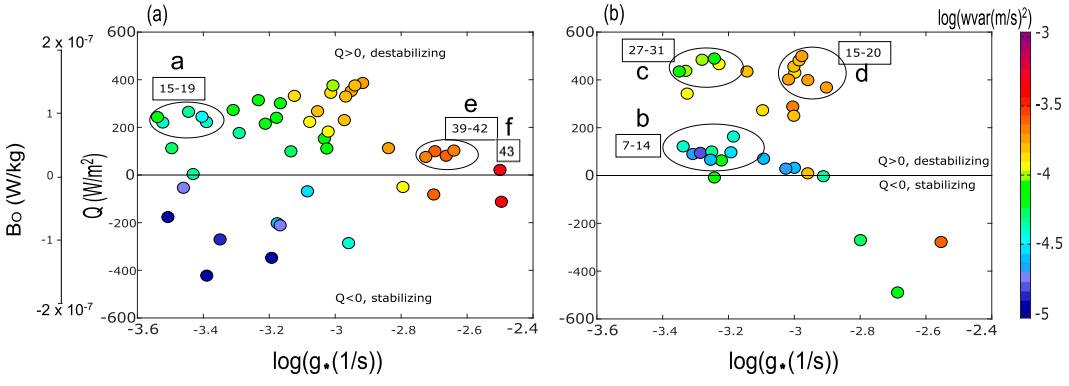

FIG. 6. Distributions in forcing space of unstratified records from consecutive sessions (a) LEO159 and (b) LEO160 (note restricted extent of the x axis compared to Fig. 5). Ellipses and letters highlight clusters of records within which forcings are quasi-steady and records have similar character of velocity/backscatter features. Numbers for records not within the clusters are omitted for clarity. Visualizations of an individual record from each cluster, shown in Fig. 7, illustrate systematic variation in qualitative organization of turbulence with location in forcing space. Color codes log(wvar).

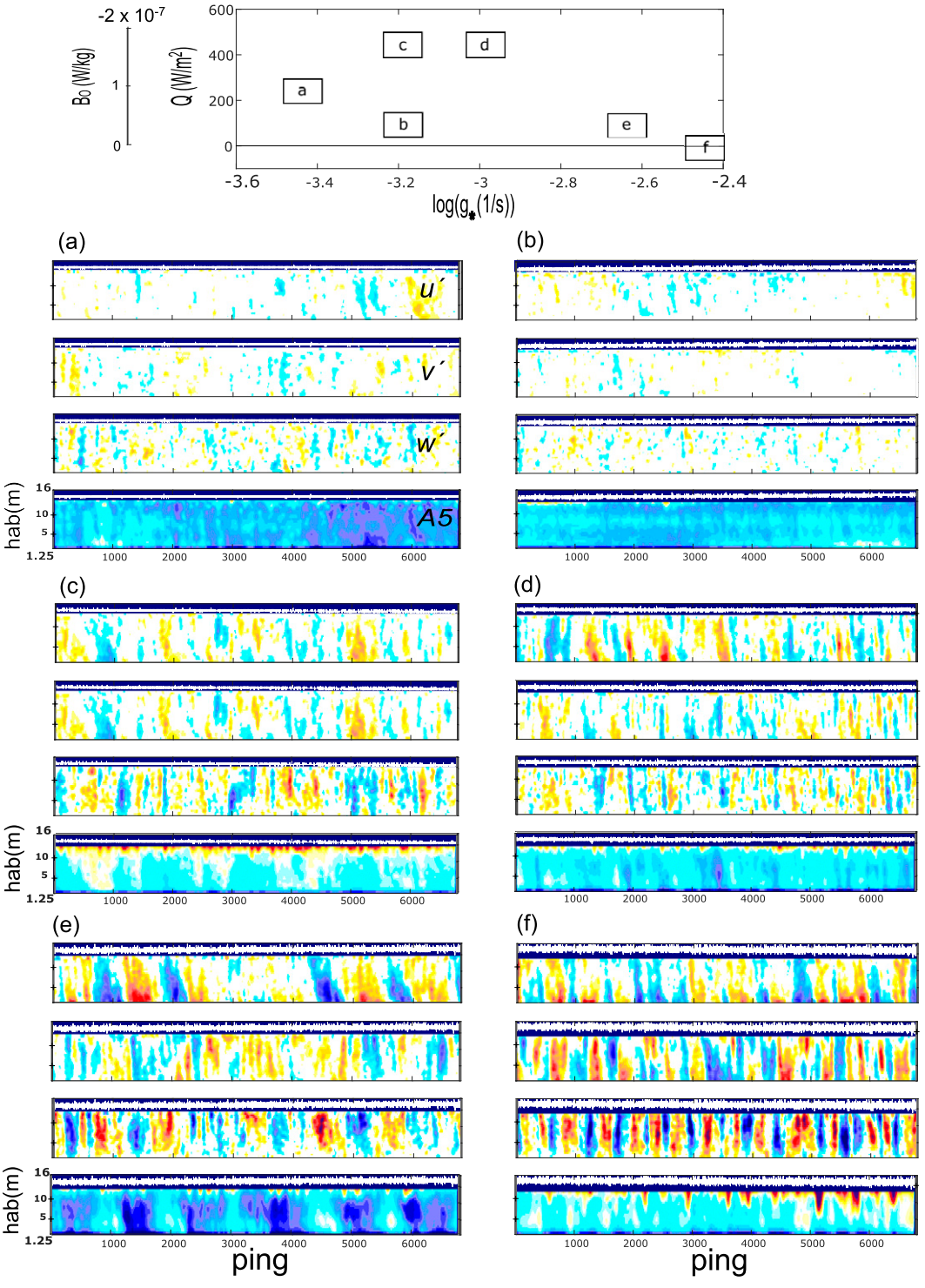

FIG. 7. (top) Map of the forcing space locations of the clusters of records shown in Fig. 6. (bottom) Characteristic records from each cluster: (a) 159.18, (b) 160.07, (c) 160.28, (d) 160.17, (e) 159.40, (f) 159.43. In all panels, velocities are in the order shown in (a), with the same velocity scales (± 10 cm s^{-1} for u', v', ± 4 cm s^{-1} for w') and the color bars used in Fig. 4. Backscatter amplitude A5 has constant range (20 units) but can differ in offset: offset 70 in (a)–(c), offset 75 in (d), and offset 80 in (e) and (f). All fields have been Hanned over three (0.4 m) range bins in the vertical and 121 (1 s) pings in time.

TABLE 1. The stress metric $[10^4 \times (\text{m s}^{-1})^2 = (\text{cm s}^{-1})^{-2}]$ defined in the text for the clusters shown in Fig. 6: added clusters define averages and standard deviations for end-member conditions of pure convection (CVN) and Langmuir supercells (LSC). Values of the stress metric significantly different from zero are highlighted in bold font.

		c: 160.27–31	d: 160.15–20		
		0.306 ± 0.170	**0.744 ± 0.265**		
CVN: 161.06–09	a: 159.15–19				
0.004 ± 0.084	0.113 ± 0.112				
		b: 160.07–14		e: 159.39–42	LSC: 043.22–26
		0.180 ± 0.211		**1.33 ± 0.364**	**2.15 ± 0.429**

characteristic record within each cluster in Fig. 6, with the general location of each cluster outlined in the upper diagram. Any of the other records within a cluster yield visualizations with character similar to that shown.

Cluster a, with an intermediate value of $Q \sim 200$ W m^{-2} and the smallest value of $\log(g_*) \sim -3.4$, has weak and disorganized velocity structures similar to those of cluster b, which has a smaller value of Q but larger $\log(g_*)$. It thus seems that in cluster b larger Stokes forcing makes up in magnitude for smaller convective forcing. Both clusters have characteristics generally similar to the CVN archetype of Fig. 4c.

Cluster c has roughly the same value of $\log(g_*) \sim -3.2$ as cluster b, but significantly larger convective forcing ($Q \sim 450$ W m^{-2}), and exhibits stronger, although still disorganized, full-depth structures, with backscatter that is dominantly of surface origin. At the same value of Q but higher values of $\log(g_*) \sim -3.0$, cluster d shows clearer signs of organized structures in velocity fields; moreover backscatter now shows clear signs of bottom as well as surface origin scatterers. In cluster e, organization as well as magnitude of turbulent velocity fluctuations continue to increase as $\log(g_*)$ continues to increase and Q to decrease, culminating in the classic LSC characteristics of record 159.43 (f).

During review, it was suggested that a quantitative measure of organizational difference would be useful, in addition to the qualitative descriptions given above. Two possibilities first considered failed to provide a useful quantitative measure of the progression of organization in moving from CVN to LSC via clusters a–e. No combination of the "organizational scores" defined by Gargett and Savidge (2020, see appendix B), provided any distinction outside error bounds, save for a sharp rise between cluster e and LSC. Distinction based on the relative magnitudes of fluctuation variances, as suggested on the basis of LES modeling by Li et al. (2004), was inapplicable because in all the present observations, vertical velocity variance is smaller than either horizontal variance. Finally, a new stress metric was explored, based on observational profiles of turbulent stresses for two cases identified as CVN (GG14, their Figs. 3e,f) and LSC (GG14, their Figs. 3a–c). A consistent difference between the two cases, found common to all examples of either, is found in the turbulent shear stress $\langle -u'w' \rangle$, where angle brackets denote time (ping) averaging over a record: the minus sign provides a positive value when downward $w' < 0$ is associated with downwind $u' > 0$. All CVN records have near zero values of this stress throughout the water column, as would be expected in convection not organized by significant mean shear and unaffected by surface waves. LSC records have much larger values that are consistently positive, clear evidence of the type of organization expected of LSC. It thus seemed possible that a metric based on $\langle -u'w' \rangle$ might provide the desired quantization of the degree of organization of large-eddy turbulent structures.

To form a stress metric for a given record, the time-averaged profile of $\langle -u'w' \rangle$ is further averaged over depth (using all range bins from 1 through slantbin, the last bin before potential sidelobe effects from the surface could appear in the slant beam data used to compute u'). Values for records within clusters vary as a result of (i) different distance to the surface (hence differences in slantbin, hence the number of bins used in the record average), dependent on both the phase of the tide and wave state; (ii) different numbers of quasi-organized structures advected past the measurement site during an individual record, dependent on the varying magnitude of crosswind tidal flow; (iii) different numbers of records in each cluster, and finally (iv) the natural variability expected of a turbulent flow. Record-averaged values of the stress metric are thus finally averaged over all records within the clusters of Fig. 4 (plus two added clusters that define representative values for CVN and LSC) and shown in Table 1 with the standard deviation within the cluster. The mean value of the metric is seen to increase continuously in moving from CVN to LSC via clusters a–e in order (although note that values for CVN and clusters a and b are statistically indistinguishable from zero, consistent with the previous conclusion that both of these clusters have characteristics generally similar to the CVN archetype of Fig. 4c). The stress metric as defined thus serves to quantify the qualitative changes in organization of the turbulent velocity fields in the representative records of Fig. 7 that are described above.

The turbulent velocity and backscatter fields of Fig. 7 demonstrate a general progression of qualitative features and an associated quantitative stress metric that together describe the changing degree of effective organization of large-eddy features with position in forcing space. However, given previous discussion of the similarities between structures resulting from sheared convection and those resulting from Stokes forcing, it still remains unclear how to apportion observed turbulent variances between the two processes anywhere between the end-members of CVN and LSC. In practice, separation would be unnecessary if means could be devised to predict some useful quantity or quantities

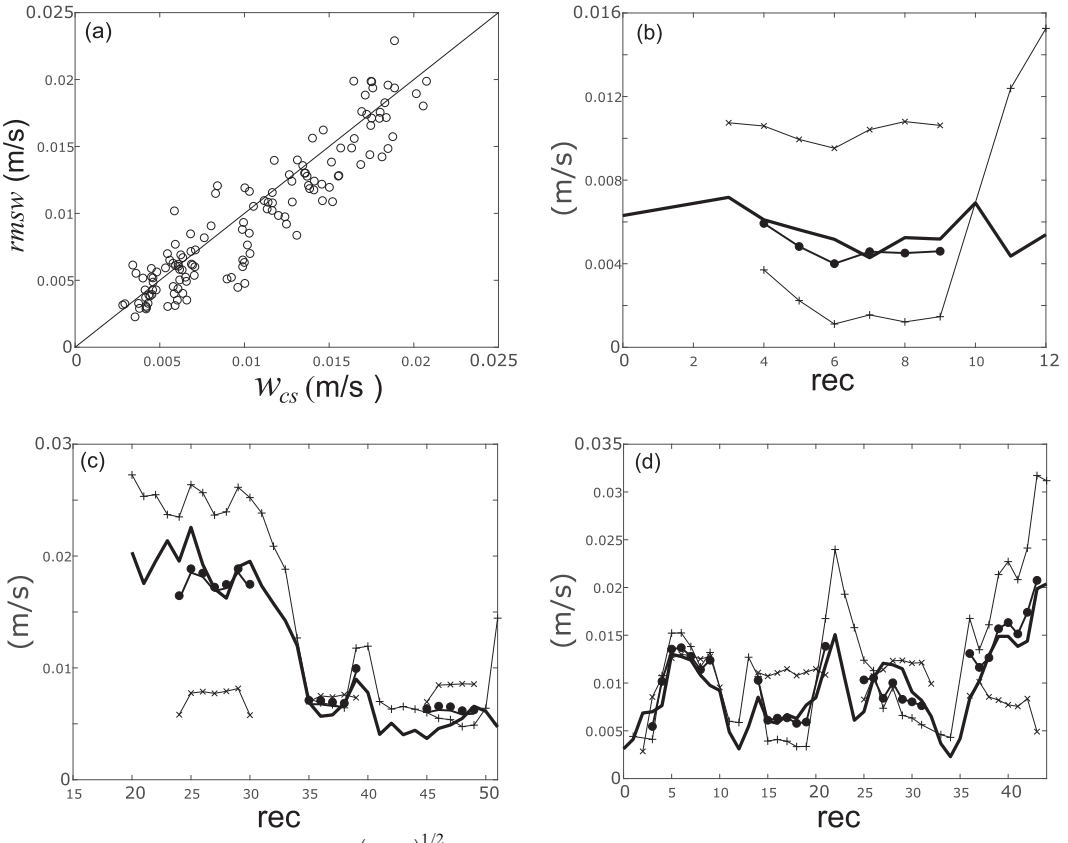

FIG. 8. (a) Dependence of rmsw = $\left(\overline{\langle w'^2 \rangle}\right)^{1/2}$ on the weighted mean scale velocity $w_{CS} = a_C w_* + a_S w_{*S}$, with $a_C = 0.35$ and $a_S = 0.6$, for good records from all sessions which have $Q > 0$. A 1:1 line is shown for reference: linear least squares fit to the data yields slope 0.95 and intercept zero. In the examples of (b) LEO161, (c) LEO043 (unstratified only after record 20), and (d) LEO159, the fundamental comparison is between observational rmsw (heavy black line) and w_{CS} (black dots connected by a line). The components of w_{CS} are also shown: convective scale velocity w_* (x marks) when $Q > 0$ and Stokes scale velocity w_{*S} (plus signs) where U_{S0} is determinable.

associated with the unseparated combination, a challenge now addressed.

4. Prediction of rmsw = (wvar)$^{1/2}$ from scale velocities associated with surface forcings

Turbulent vertical velocity variance wvar has been the primary quantitative measure used for the strength of turbulence in many studies of the OSL. Is it possible to predict the obvious pattern of wvar magnitude seen in the cases of mixed convective and Stokes forcings observed in the measurements of Fig. 5?

The method explored here is to use scale velocities that separately characterize unstable convection and Stokes wind-wave forcing to predict observed values of root-mean-square turbulent vertical velocity rmsw = wvar$^{1/2}$ at times when both forcings are present simultaneously. From extensive atmospheric literature, the appropriate scaling velocity for convection is given by

$$w_* = (B_o H)^{1/3} = \left(\frac{\alpha g}{\rho_o C_v} QH\right)^{1/3}, \tag{4}$$

where H is the depth of an unstratified water column.

As a scale velocity for Stokes-forced turbulence, I will use

$$w_{*S} \equiv \left(u_*^2 U_{S0}\right)^{1/3}. \tag{5}$$

This particular form, suggested by both theory (Smith 1996) and LES (Skyllingstad 2000; Min and Noh 2004; Grant and Belcher 2009; Harcourt and D'Asaro 2008), involves underlying assumptions that are in accord with various features of LC observations, as elucidated by GG14.

The simplest approach to scaling turbulence driven by mixed convective/Stokes forcings is a weighted sum of the two scale velocities

$$w_{CS} = a_C w_* + a_S w_{*S}, \tag{6}$$

since such a scaling approaches an end limit of one dominant scale velocity when the other becomes small. The appropriate choice of weights is made by choosing coefficients necessary to give rough agreement with the two end-members, assuming that w_* dominates if w_{*S} is small, w_{*S} if w_* is small. These initial weights are then slightly modified

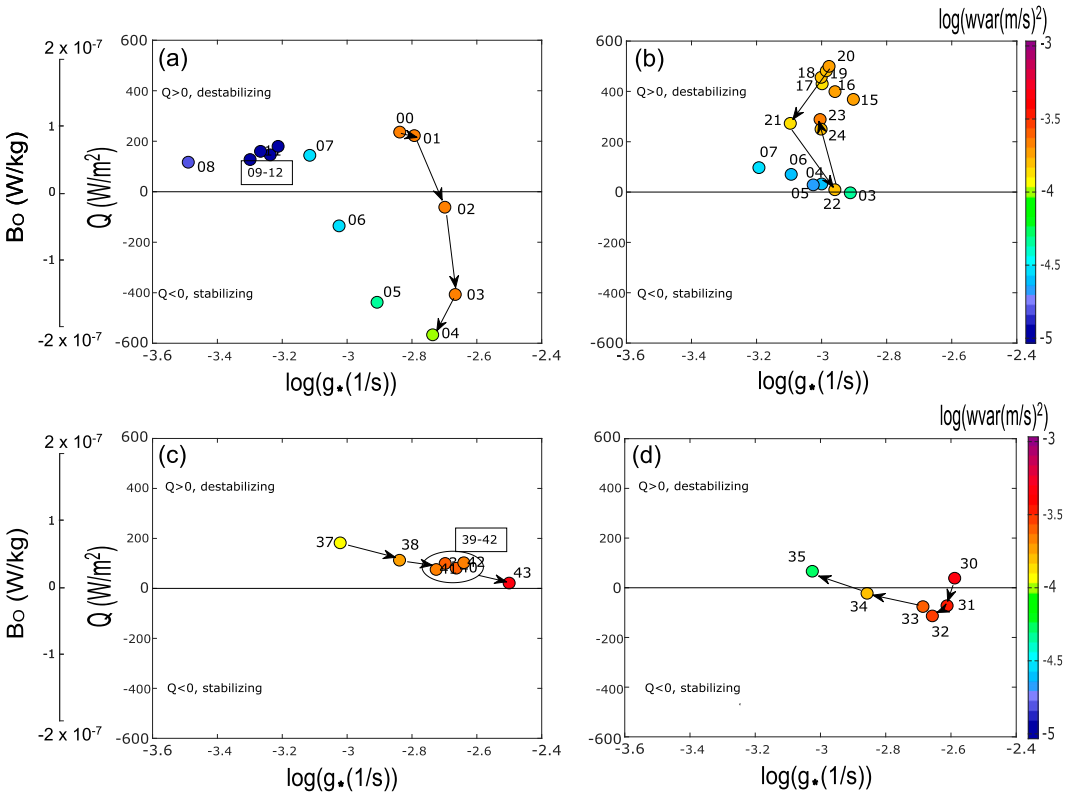

FIG. 9. Portions of (a) LEO128 and (b) LEO160 in forcing space, illustrating time-dependent surface buoyancy forcing at relatively constant Stokes forcing and portions of (c) LEO159 and (d) LEO043, illustrating time-dependent Stokes forcing at relatively constant Q. These results suggest a longer turbulence adjustment time scale associated with buoyancy forcing change than wind-wave forcing change.

in order to optimize the observed linear relationship of rmsw to w_{CS} over all available data. Figure 8a shows the relationship (6) with $a_C = 0.35$ and $a_S = 0.6$, with a 1:1 line shown for reference: a linear least squares fit to the data produces a slope of $0.95 \sim 1$, with intercept zero. The other plots of Fig. 8 show measured values of rmsw, determinable values of w_{*S} (i.e., where U_{S0} can be calculated) and determinable values of w_* (i.e., where $Q > 0$) for the two end-member records LEO161 (Fig. 8b) and LEO043 (Fig. 8c) used to set a_C and a_S, respectively, as well as LEO159 (Fig. 8d), a session exhibiting a wide range of combinations of convective and Stokes forcing, as seen in Fig. 6a. The scale velocity w_{CS} reasonably scales observed rms vertical velocity for both CVN in LEO161 and LSC in LEO043, as well as most of the individual records of LEO159, from CVN (records 15–20) through mixed forcings (records 4–10) to LSC (records 36–43).

While a successful scaling for rmsw over a full range of mixed forcings has been demonstrated, it should be pointed out that use of U_{S0} as presently derived from observations and widely used in the literature in the definition of the LC scale velocity w_{*S} is a disadvantage because of a range of issues in determining its value in all conditions (section 2a). Consideration of alternate forms for near-surface Stokes drift (e.g., GG14, their Fig. A3; Harcourt and D'Asaro 2008) for use in defining a "best" scaling velocity to use for LC is beyond the scope of this paper, but will be addressed in a subsequent study.

5. Effects of time-dependent forcing

Focus thus far has been on characterizing and quantifying turbulence during conditions with relatively constant wind-wave and destabilizing buoyancy forcings (hence the clusters in Figs. 6 and 7 in which both forcing metrics are approximately constant for several hours). However, in the real world, surface buoyancy forcing normally has a strong diurnal cycle, with overnight heat loss usually followed by (often large) stratifying heat flux during daytime hours, while wind stress and wave fields vary on erratic time scales associated with frontal passages and storms. It is thus of interest to see what information is offered by forcing space locations of records during times of strongly time-dependent forcing.

First consider change predominantly in surface heat (buoyancy) flux, as seen in the two examples of Figs. 9a,b. Figure 9a shows a portion of LEO128 which begins with two records (00 and 01) exhibiting characteristics similar to those in Fig. 7e, i.e., structures similar to LSC but with slightly less

organization and somewhat weaker turbulent velocities than the LSC end-member. During a period (records 00–04) with nearly constant g_* (constant Stokes forcing), the surface heat flux reverses sign, becoming increasingly stabilizing, yet without noticeable change in wvar until approximately record 4, 4–6 h after the change in buoyance forcing begins. Thus a period of ~4–6 h of stabilizing surface heat flux appears necessary to significantly diminish existing turbulence.

A second example of the slowness of response to changes in heat flux forcing is seen in LEO160 (Fig. 9b) when a sharp but short-lived (only in record 22) decrease in destabilizing heat flux leaves wvar relatively unchanged over the period of records 21–24. A decrease of Q by over 200 W m^{-2} but lasting only ~2 h was not sufficient to significantly decrease the magnitude of wvar. This slow response to change in heat flux forcing magnitude makes the wvar of record 22 an outstanding mismatch to the other records (03–07) in the same area of forcing space.

In contrast, response to change in magnitude of wind-wave (Stokes) forcing as quantified by g_* is demonstrably faster, as seen in Figs. 9c,d, respectively, portions of LEO159 and LEO043 with relatively constant values of Q. The portion of LEO159 starts with a record (37) that has full depth but weak and disorganized structures, but as g_* increases, these become more organized and stronger in magnitude (see record 40 in Fig. 7e) culminating in LSC (record 43, Fig. 7f). The opposite progression is seen in Fig. 9d, where record 043.30 starts as LSC, but subsequent records steadily decrease in both organization and wvar as g_* decreases, behavior consistent with their movement in forcing space (note that these are the same records which move in an *inconsistent* direction with respect to La in the regime diagram of Fig. 3). In both of these cases, record-to-record changes keep the magnitude of wvar in agreement with the overall distribution seen in Fig. 5. Thus the time for turbulence adaptation to changes in Stokes forcing appears to be less than 2 h.

These time scale results are in general agreement with order of magnitude estimates presented by GG14, based on large-eddy overturning time scales calculated using H and the vertical scale velocities used in section 4 for either Langmuir circulation or destabilizing convection. Their results suggested an adjustment time for wind-wave forced turbulence shorter than the record length (so that Langmuir turbulence averaged over the 2-h record period would be effectively in steady state with the forcing at the time) while that for convection was substantially longer. Although their calculations did not encompass mixed turbulence, i.e., that forced by a combination of wind-wave and convective forcings, the present results suggest that an appropriate adjustment time is the "fast" Langmuir adjustment time (<2 h) if wind-wave forcing change dominates, and the "slow" (4–6 h) convective adjustment scale if the dominant change is in buoyancy forcing.

The diurnal cycle of surface buoyancy flux forcing has a daytime period of stabilizing forcing that is typically shorter than that of destabilizing (convective) nighttime forcing. Coupled with slower adjustment time to changes in the surface flux, this implies that the state of turbulence during daytime hours is rarely in steady-state and, particularly early in the day, is often a strong function of its state at the end of the previous night.

Before leaving Fig. 9, note the cluster of records marked 9–12 in Fig. 9a. In all the sessions examined, this is the sole cluster with variance (extremely weak, as seen here and, partially hidden, in Fig. 5) that disagrees with its position in forcing space. It appears likely that the cause is the presence of stratification. Evidence for stratification comes first from the observation of significant vertical shear in horizontal mean velocity, beginning in record 9 and persisting until record 17 (records 13–17, with stratifying heat flux, were omitted from Fig. 9a): such shear is often associated with density stratification. In the present case, any stratification must be associated with salinity, since the temperature difference remains near zero. Unfortunately, there were no continuous salinity measurements at the site: a CTD at the node was operated manually (and sporadically) only during daytime working hours at the LEO observatory. Equally unfortunately, records 9–12 were at night. However, the first two subsequent daytime CTD profiles, both taken during record 13, show a step change in density within the water column at approximately the level of observed horizontal velocity shear. The density step moves progressively toward the bottom (as does the shear layer) and is last seen in a CTD taken during record 15: thereafter the water column has an unstratified profile above ~1 m above bottom. No steps were found in available CTDs within, immediately before, or immediately after any of the other sessions used here, leading to the conclusion that salinity-induced stratification caused the apparent failure of the forcing regime diagram in this single cluster of records, emphasizing the importance of complete observations of water column density structure.

6. Discussion and conclusions

Various forms of regime diagrams have been proposed for use in diagnosing the structure and strength of upper-ocean turbulence generated through direct surface forcing by destabilizing buoyancy flux and/or wind stress, plus the inevitable waves driven by wind stress. A major conclusion of the present work is that all of the proposed forms for regime diagrams share significant shortcomings. Perhaps the most fundamental is the use of ratios of scaling parameters to form what are supposedly definitive descriptors. It has been clearly demonstrated that turbulence characteristics can depend not only on the value of a given ratio, *but on how that ratio is achieved*.

An alternate diagnostic proposed and explored here is that of a forcing space. With the assumption that surface freshwater flux is either not present or insignificant, a first dimension is surface buoyancy flux B_o (of either sign) determined from surface heat flux Q. The second dimension is g_*, a growth rate for Langmuir circulation in an unstratified fluid. While g_* uses two parameters, mean shear and Stokes shear, it does so in a theoretically derived form (Leibovich 1977) that incorporates the reality that it is almost never

possible to separate turbulence of a classical stress-driven boundary layer from Langmuir turbulence in the upper ocean, because imposition of significant surface wind stress concurrently both drives mean flow and generates surface waves. It is this intimate relationship between the two forms of wind stress driving (with small-scale turbulence from the shear boundary layer acting as a vorticity source for the Stokes vortex force even before any additional source due to wave breaking) that is likely at the root of the rough proportionality between U_{S0} and u_*, hence the statistically constant La that is a consistent feature of reported ocean observations.

Because the basic structure of large eddies associated with convection in the presence of mean shear is the same as that of Langmuir circulation, when these two mechanisms are present together they cannot be separated by identifying distinctive structures. Instead, in such mixed forcing cases it has been shown that, provided forcing conditions are roughly constant for several hours, location in the upper half-plane of $\{B_o, g_*\}$ forcing space predicts not only qualitative features of observed turbulent large eddies, but the value of a new quantitative metric based on averaged turbulent stress $\langle -u'w' \rangle$, as both range between those characteristic of end members of pure convection and Langmuir supercells. Finally, it has been demonstrated that in forcing conditions where the convective scale velocity w_* exists ($Q > 0$) and surface Stokes drift velocity U_{S0} can be computed, allowing calculation of a Stokes scale velocity w_{*S}, a linear composite of the two scale velocities generally provides an excellent estimate of the observed rms turbulent vertical velocity associated with the mixed forcing.

Surface layer forcing conditions are frequently *not* steady for extended periods of time. When forcings are not steady, it has been shown that adjustment to rapid change in only wind-wave forcing (as characterized by g_*) is itself rapid, essentially within the 2 h averaging time of records. In such conditions, the form and strength of turbulence are effectively in steady state under the applied forcing. In contrast, adjustment to rapid change in surface buoyancy forcing is slower, on the order of 4–6 h in the case of night-to-day change in sign of Q. Rapid change in surface buoyancy forcing typically occurs during periods when heat flux forcing changes sign during the diurnal cycle. At such times, turbulence is not steady state, but instead depends on the previous history of forcing.

A striking feature of the overall distribution of the observations in forcing space shown in Fig. 5 is the existence of noticeable data "holes." In the lower half of Fig. 5, the region with no data points at large values of stabilizing $Q < 0$ and small g_* is likely an artifact resulting from the finite noise level of the vertical velocity measurement. However, in the upper half-plane of mixed convective and wind/wave forcing, there are no records in the region of large g_* and large Q (of either sign), nor that of small g_* and large $Q > 0$. These holes arguably arise through characteristics of the forcings, the first because LSC (large g_*) events at LEO occur during prolonged storms when normally heavy cloud cover greatly reduces the magnitude of surface heat fluxes,

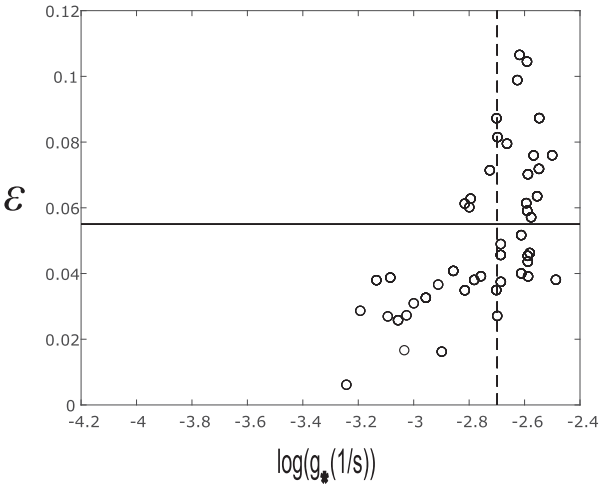

FIG. 10. Spectral wave steepness parameter ε defined by Banner et al. (2000) plotted against the logarithm of g_*, growth rate of Langmuir circulations in an unstratified fluid as derived theoretically by Leibovich (1977). Records plotted have a nonstratified water column, waves are identified as actively wind-forced waves, and $|Q| < 100$ Wm^{-2}. The solid horizontal line at $\varepsilon = 0.055$ is the value that Banner et al. (2000) identify as the onset of breaking of waves at or near the peak of a wind-wave spectrum. The vertical dashed line is at $\log\left(g_*^{\text{crit}} = 2 \times 10^{-3}\ \text{s}^{-1}\right)$, the value that Gargett and Savidge (2020) found marked a transition between states with and without LSC. The coincidence of these transitions implies a strong role for wave breaking in generation of LSC.

the second because surface heat flux is a function of wind speed (Fairall et al. 2003), hence restricted in magnitude in conditions of low wind stress/low wave state. It will be interesting to discover whether these holes are filled when surface forcing conditions are more extreme than those encompassed by the present observations.

Using data from the LEO043 storm event and from storm events at a deeper site off the coast of Georgia, Gargett and Savidge (2020) suggested that LSC essentially disappear below a critical value of $g_* = g_*^{\text{crit}} \sim 2 \times 10^{-3}\ \text{s}^{-1}$ [$\log(g_*) \sim -2.7$]. Figure 5 shows that this conclusion is a reasonable one *provided* that during and after the transition through g_*^{crit}, Q remains $< \sim 100$ W m^{-2} (or $B_o < 4 \times 10^{-8}$ W kg^{-1}, as was the case with the data used by Gargett and Savidge 2020). For example, moving to the left with $|Q| < \sim 100$ Wm^{-2} in Fig. 5, wvar of $O[10^{-3}]$ (m s^{-1})^2 associated with LSC at $\log(g_*) > -2.7$ decreases by more than an order of magnitude by $\log(g_*) = -3.0$ and remains low for still smaller values of g_*. It is interesting to speculate on a physical process associated with the transition in such cases, i.e., where heat flux likely plays an insignificant role, hence the observed difference must be related to difference in wave forcing. In this regard, Fig. 10 shows ε, a spectral peak wave steepness parameter defined by Banner et al. (2000), as a function of $\log(g_*)$. It is clear that the point where g_* exceeds g_*^{crit} coincides roughly with the point where ε exceeds the value of 0.055 that Banner et al. (2000) claim marks the onset of breaking of wind-driven waves at or near the spectral peak. The

coincidence of these transitions supports the suggestion by Gargett and Savidge (2020) that already paired vorticity supplied by the horizontal velocity "scars" of breaking waves is a more effective input of the vertical vorticity necessary for the Stokes force than is the randomly oriented vertical vorticity of a classical sheared boundary layer. While the fundamental process(es) underlying the observed transition in purely wave-forced turbulence at g_*^{crit} is an interesting subject for future research, it should be recognized that a similar transition in g_* that also moved toward high heat loss (e.g., toward states like clusters c and d in Fig. 7) would not show such a sharp cessation of LSC, but the progressive decrease in turbulence organization and strength documented in Fig. 7.

The observations discussed here have significant consequences for numerical modeling of OSL turbulence. Studies focused solely on Langmuir turbulence, i.e., with no surface buoyancy forcing, should be run at or near the value of La $\sim O(0.1)$ that is reliably exhibited by observations. However, pure wind/wave forcing, i.e., with $B_o \propto Q \sim 0$, is the exception rather than the rule in the real ocean, occurring mostly when the strong diurnal cycle in buoyancy forcing normally present is reduced by cloud cover during storms. During the often extensive periods between major storms, turbulence in the OSL is influenced both by nighttime convection and by stabilizing daytime heating: thus further LES studies of mixed forcings, adding to those of Min and Noh (2004) and Walker et al. (2016), are recommended. Finally, to date most models involving Langmuir turbulence are run to steady state. While it has been demonstrated that OSL turbulence can be considered to be in quasi-steady state under changes in wind-wave forcing, this is not an acceptable assumption when change in buoyancy forcing plays a significant, even if partial, role. LES case studies of simplified time-dependent scenarios with mixed forcings would be useful in determining a reliable "decay time" of mixed layer turbulence upon the switch to stabilizing daytime heat gain and a (likely different) "growth time" following the opposite switch to destabilizing nighttime heat loss, plus how these time scales depend on the form/strength of turbulence present before a change in buoyancy forcing. The night-to-day time scale would be particularly useful to biologists seeking to understand the mixing environment of phytoplankton during sunlit hours, since the present results indicate that this environment can depend strongly upon conditions the previous night.

In conclusion, it should be acknowledged that the present exploration of the utility of a forcing space uses data from a shelf site where, under certain wind directions, the presence of a nearby shoreline allows development of steady-state mean flows (Grosch and Gargett 2016), potentially allowing turbulent structures that are more organized than those typical of the deep ocean mixed layer, where imposition of steady wind instead produces rotating mean flow and Langmuir turbulence (McWilliams et al. 1997). It is thus essential that data similar to that presented here be obtained in this latter case. While standard observational procedures are available for the necessary wind/wave forcing fields in the deep ocean environment, the outstanding challenge is to obtain time-continuous information on large-scale turbulent structure and intensity similar to that used here. A short exploratory deployment of a standard ADCP looking upward from a subsurface float on a stable offshore mooring (R. E. Thomson 2010, personal communication) recorded fluctuating tilts that were encouragingly small. With engineering to reduce mean tilts (which averaged 0.5°–1°), use of a VADCP in this configuration could perhaps provide the necessary direct turbulence information.

Acknowledgments. Support for the LEO deployment by the U.S. National Science Foundation (OCE0136403 and OCE0927724) and NOAA (NA06RU0139) is gratefully acknowledged, as is the technical support of Chris Powell and Shuang Huang. I thank Rick Thomson for his role in deploying an offshore upward-looking ADCP, and Nobu Suzuki and Johannes Gemmerich for helpful discussions during the writing of this manuscript. Reviewer comments were appreciated. As always, I acknowledge the many contributions of my late colleague Chester Grosch to the topics discussed here.

Data availability statement. Data used are available on Zenodo (doi: 10.5281/zenodo.5048343).

APPENDIX

Correction for Missing Variance in Stokes Function and Stokes Shear Function

GG14 describe derivation of a surface wave displacement spectrum from measurements of vertical velocity in a vertical range bin taken as close as possible to the mean surface (a distance dependent upon surface wave height). The derivation involves a response function that rises steeply for $f < f_L = 0.06$ Hz and, in cases with large waves, also for $f > f_M = 0.4$ Hz (for discussion and examples of the response function in low and high wave states, see the appendix of GG14). The range of acceptable displacement spectral estimates is thus taken as $f < f_L < f_M$. The resulting displacement spectrum is used in the expression of Kenyon (1969) to derive a Stokes function whose integral over frequency is the Stokes velocity (hence use of the term function rather than spectrum) as a function of x_3. The vertical derivative of this is the associated Stokes shear function.

Figure A1 shows displacement spectra (Fig. A1a) and associated surface ($x_3 = 0$) Stokes functions (Fig. A1b) derived for all records in LEO043. In both panels, the left vertical line is at the spectral estimate corresponding to $f_L \equiv \text{ceil}(0.06 \text{ Hz}/\delta f)$ where δf is the spectral frequency resolution: f_L is taken as the low-frequency limit of integrations for wave height and surface Stokes drift velocity. The right solid vertical line in both is at the spectral estimate corresponding to $f_M \equiv \text{floor}(0.4 \text{ Hz}/\delta f)$, taken as the upper-frequency limit of integration for both variables. Spectral/function peaks are sought only within this range. The dashed vertical line in (Fig. A1b) is at $f_M - 2\delta f$. Records in which the surface Stokes function peaks at (or below) this

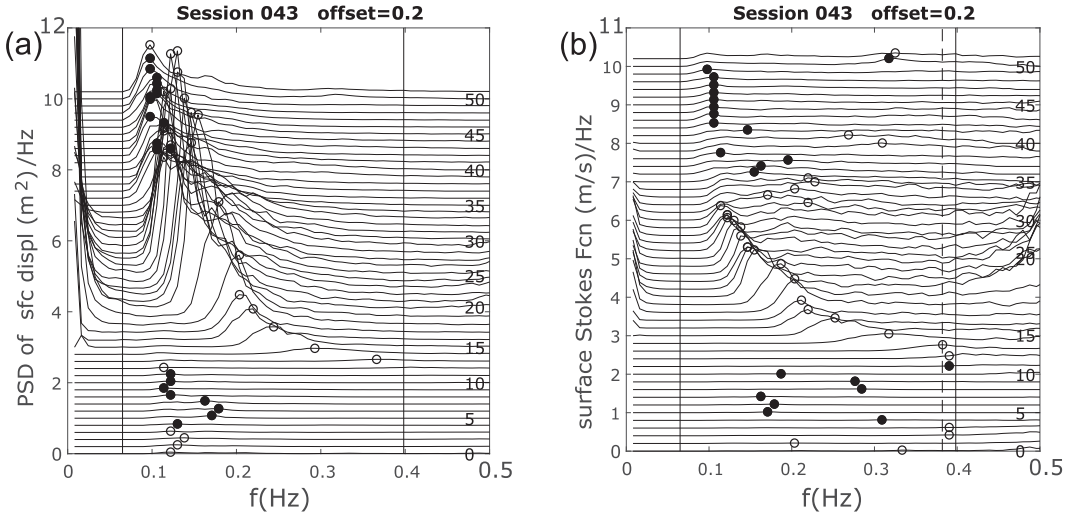

FIG. A1. (a) Displacement spectra and (b) surface Stokes functions for all records of LEO043. Black dots mark peaks of displacement spectra/Stokes functions for records in which an ECMWF criterion (Bidlot 2020) identifies the displacement peak wave as not wind forced.

frequency are considered to have a defined peak (i.e., the Stokes function decreases for at least two frequency estimates beyond the peak but before f_M). Stokes functions with peaks at frequencies above this limit are considered undefined and/or potentially affected by noise, hence U_{S0} is indeterminate.

Because the Stokes spectral function is weighted to high frequencies relative to the displacement spectrum, it is desirable to correct measured spectra for missing variance from frequencies above f_M. As discussed in section 2a, corrections in published articles have been done using various assumptions about the wave spectral form above f_M. Because wind-forced waves in the present data achieve the high wavenumber Toba (1973) f^{-4} form at frequencies above the displacement spectral peak (not shown), the present correction uses a minor variation of a model originally introduced by CVG, who appended to the measured spectral value at f_M a "tail" with slope transitioning from -4 at f_M to -5 at a wave-breaking frequency $\omega_B = 2\pi f_B = 0.0061 g/u_*$ determined by Forristall (1981). CVG reasonably argued that once waves break they no longer contribute to the first-order nonlinearity that is Stokes drift, hence terminated the added variance calculation at f_B.

As discussed above, the present observations derive surface wave height from vertical velocity measured in a vertical range bin as close as possible to the mean surface, a process that involves a transfer function that rises at high frequencies, the more steeply the further the measurement is below the mean sea surface. For frequencies above 0.4 Hz, this transfer function is near 1 for low wave heights, but increases when larger waves force the measurement bin further from the surface, introducing the likelihood of error due to noise amplification in such cases. As a result, the measured spectrum is used only to f_M, and a high-frequency extension for $f_M < f < f_B$ is made using the deterministic level of the Toba spectrum at f_M, as follows.

Expressed in radian frequencies, the Toba version of the wave height spectrum above ω_P, the peak frequency of the displacement spectrum, is

$$\phi_{\mathrm{Toba}}(\omega) = \alpha_{\mathrm{Toba}} g u_* \left(\frac{\rho_w}{\rho_{\mathrm{air}}}\right)^{1/2} \omega^{-4}. \tag{A1}$$

Forristall (1981) reported two distinct ranges in his measurements, ω^{-4} from the spectral peak out to a sharp change (to ω^{-5}) at $\omega = \omega_B$. The Toba form is thus used here for frequencies $\omega_M < \omega < \omega_B$, without the gradual change in

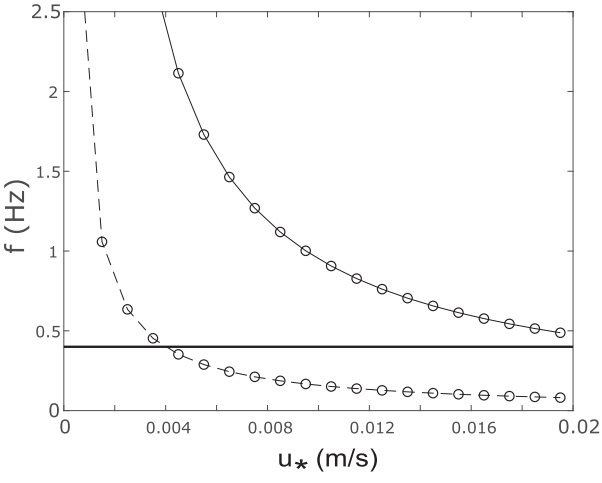

FIG. A2. Significant frequencies as functions of u_* over the range of u_* observed at LEO. The horizontal line is $f_M = 0.4$ Hz, the maximum accepted frequency for measured wave displacement spectra at LEO. The black solid curve is the wave breaking frequency f_B of Forristall (1981). The black dashed curve is the frequency f_W above which ECMWF declares waves to be wind forced.

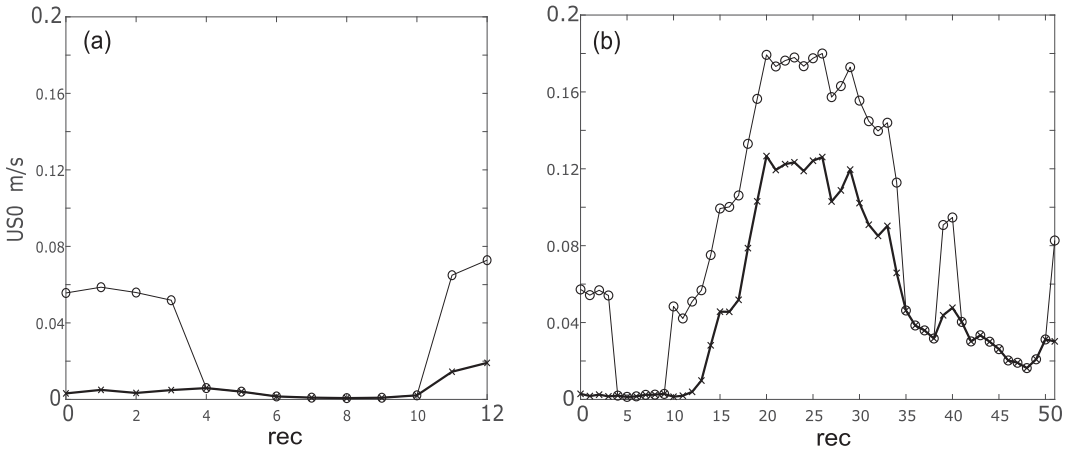

FIG. A3. For sessions (a) LEO161 and (b) LEO043, surface Stokes drift velocity U_{S0} uncorrected (heavy line) and corrected with the present algorithm (light line). Records with equal estimates are those that do not meet the ECMWF criterion for wind-forced waves.

slope used by CVG. The resulting Stokes spectral function at the surface is given by

$$\begin{aligned} U_{S0} = U_S(x_3 = 0) &= 2\int_0^{\omega_M} \phi_s(\omega)\omega k \frac{\cosh 2\,kH}{2\sinh^2 kH}\, d\omega \\ &\quad + \frac{2}{g}\int_{\omega_M}^{\omega_B} \alpha_{\mathrm{Toba}} g u_* \left(\frac{\rho_w}{\rho_{\mathrm{air}}}\right)^{1/2} \omega^{-4}\omega^3 d\omega \\ &= \mathrm{US0}_M + A_{\mathrm{Toba}}\int_{\omega_M}^{\omega_B} \omega^{-1}\, d\omega \\ &= \mathrm{US0}_M + A_{\mathrm{Toba}}(\ln\omega_B - \ln\omega_M) \qquad \text{(A2)} \end{aligned}$$

where $\phi_s(\omega)$ in the first term is the measured surface wave height spectrum and the second term uses $\phi_{\mathrm{Toba}}(\omega)$ in the deepwater form[A1] of the Stokes function (see the appendix of GG14). $\mathrm{US0}_M$ is the measured part of the variance and $A_{\mathrm{Toba}} = 2\alpha_{\mathrm{Toba}} u_* (\rho_w/\rho_{\mathrm{air}})^{1/2}$ is known, given a (record average) value of u_* and a value for the Toba constant, here taken as $\alpha_{\mathrm{Toba}} = 0.11$.[A2] The corrected value U_{S0} is thus

$$U_{S0} = \mathrm{US0}_M + A_{\mathrm{Toba}} \ln\left(\frac{\omega_B}{\omega_M}\right) = \mathrm{US0}_M + A_{\mathrm{Toba}} \ln\left(\frac{f_B}{f_M}\right). \qquad \text{(A3)}$$

As u_* increases, f_B decreases (solid curve in Fig. A2), eventually reaching frequencies $f_B \le f_M$. For such situations, absent in the present dataset, calculation of $\mathrm{US0}_M$ would be halted at f_B.

Figure A3 shows uncorrected and corrected values of U_{S0} for records in sessions LEO161 and LEO043. Records where the values are the same in these plots are those affected by an unaddressed problem with previous and present forms of variance correction, namely, the question of how to correct the variance when waves are *not* wind-forced waves, but rather decaying remnants of a previous wind event and/or swell, conditions usually associated with low and/or decreasing wind stress. To identify such cases, I use the criterion of the ECMWF [Bidlot 2020, Eq. (1)] which declares that waves are considered subject to forcing by wind when

$$1.2 \times 28\left(\frac{u_*^a}{c}\right)\cos(\theta - \phi) > 1,$$

where u_*^a is the air-side wind stress velocity, the phase speed of the spectral peak wave is $c = \omega/k = \omega g/\omega^2 = g/\omega = g/(2\pi f)$, and ϕ and θ are respectively the directions (to) of the wind and the wave. Using this expression for c[A3] and assuming wind-aligned waves[A4] yields $f_W = g/[1.2(28)2\pi u_*^a] = g(\rho_a/\rho_w)^{1/2}/[1.2(28)2\pi u_*]$ as the frequency f_W above which waves are wind forced, shown as the dashed curve in Fig. A2. For values of $u_* < \sim 0.004$ m s^{-1}, none of the observed spectral range can be considered as wind forced, hence adding a wind-forced extension is unjustified. I chose not to correct U_{S0} for such records since it is unclear

[A1] Waves of frequency 0.4 Hz or greater are effectively deepwater waves in 15-m water depth, justifying use of a high wavenumber extension based on deepwater forms.

[A2] The Toba coefficient is often taken to be 0.096, the simple mean of all values given in Table 2 of Battjes et al. (1987), eight estimates ranging from 0.02 to 0.13 and increasing chronologically with date of publication. Many are from limited fetch studies and the first is a laboratory study. More recently, Resio et al. (2004) and Romero and Melville (2010) both found the Toba coefficient to vary somewhat with wave age. The value 0.11 used here assumes a wave age of ~26.

[A3] Phase speeds of intermediate waves, often typical at LEO, diverge from those of deepwater waves only for frequencies less than ~0.1 Hz, a peak frequency not reached until values of u_* in excess of 0.016 m s^{-1}. Thus the deepwater approximation is adequate for the values of $u_* < 0.004$ m s^{-1} where f_W exceeds f_M, hence by the ECMWF criterion the measured spectrum is not associated with wind-forced waves.

[A4] The assumption of wind-aligned waves provides a lower bound over the entire range, since if waves are not aligned with the wind, the factor $\cos(\theta - \phi) < 1$ requires an even larger frequency $f_W^n = [f_W/\cos(\theta - \phi)] > f_W$.

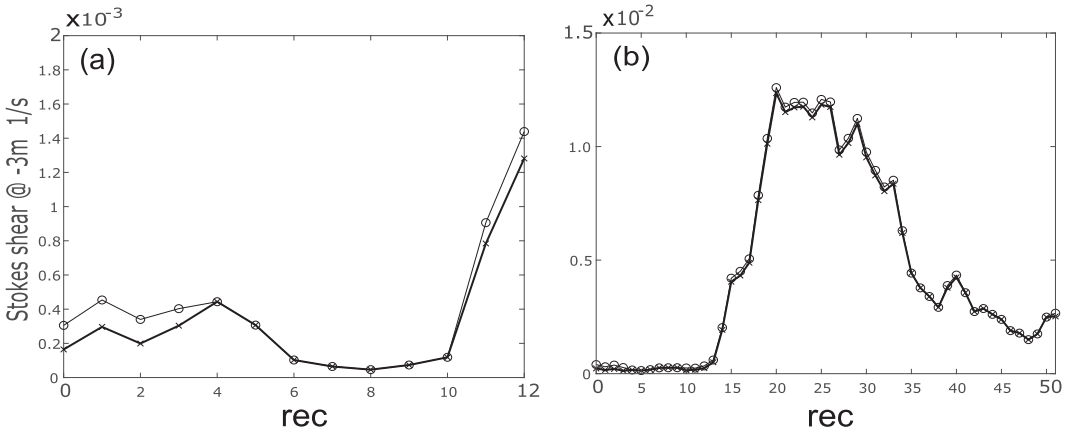

FIG. A4. For sessions (a) LEO161 and (b) LEO043, Stokes shear at $x_3 = -3$ m uncorrected (heavy line) and corrected (light line) with the present algorithm.

what an appropriate extension would be under these circumstances (while the "correct" value presumably lies somewhere between the uncorrected and corrected values, specific investigation of the high-frequency spectral form of waves that are not being actively wind forced is necessary to resolve this issue). In Fig. A1, white/black dots denote LEO043 records that are/are not wind forced by the ECMWF criterion, hence the associated values of U_{S0} do/do not include estimated missing variance.

Stokes velocity at a depth $x_3 < 0$ below the surface is given by

$$U_S(x_3) = 2\int_0^{\omega_M} \phi_s(\omega)\omega k \frac{\cosh 2k(x_3 + H)}{2\sinh^2 kH} d\omega + A_{\mathrm{Toba}} \int_{\omega_M}^{\omega_B} \omega^{-1} \exp\left[2\left(\omega^2/g\right)x_3\right] d\omega$$

again using the deepwater form of depth variation in the second term. Stokes shear at x_3 is thus given by

$$\frac{dU_S}{dx_3} = \left(\frac{dU_S}{dx_3}\right)_M + A_{\mathrm{Toba}} \int_{\omega_M}^{\omega_B} \omega^{-1} 2\left(\frac{\omega^2}{g}\right) \exp\left[2\left(\omega^2/g\right)x_3\right] d\omega, \tag{A4}$$

from which a straightforward calculation yields the corrected Stokes shear

$$\frac{dU_S}{dx_3} = \left(\frac{dU_S}{dx_3}\right)_M + \frac{A_{\mathrm{Toba}}}{2x_3}\left\{\exp\left[2\left(\omega_B^2/g\right)x_3\right] - \exp\left[2\left(\omega_M^2/g\right)x_3\right]\right\}. \tag{A5}$$

As seen in Fig. A4b, the value of Stokes shear at the depth $x_3 = -3$ m used in calculating g_* is almost unaffected by the loss of variance correction, a direct result of the choice by GG14 of this depth as the shallowest at which the Stokes shear spectrum was bounded within

$$f < f_M \simeq 0.4 \text{ Hz}.$$

REFERENCES

Banner, M. L., A. V. Babanin, and I. R. Young, 2000: Breaking probability for dominant waves on the sea surface. *J. Phys. Oceanogr.*, **30**, 3145–3160, https://doi.org/10.1175/1520-0485(2000)030<3145:BPFDWO>2.0.CO;2.

Battjes, J. A., T. J. Zitman, and L. H. Holthuusen, 1987: A reanalysis of the spectra observed in JONSWAP. *J. Phys. Oceanogr.*, **17**, 1288–1295, https://doi.org/10.1175/1520-0485(1987)017<1288:AROTSO>2.0.CO;2.

Belcher, S. E., and Coauthors, 2012: A global perspective on Langmuir turbulence in the ocean surface boundary layer. *Geophys. Res. Lett.*, **39**, L18605, https://doi.org/10.1029/2012GL052932.

Bidlot, J.-F., 2020: Official IFS documentation CY47R1—Part VII: ECMWF Wave Model. ECMWF, 114 pp., http://dx.doi.org/10.21957/31drbygag.

Clarke, A. J., and S. Van Gorder, 2018: The relationship of near-surface flow, Stokes drift and the wind stress. *J. Geophys. Res. Oceans*, **123**, 4680–4692, https://doi.org/10.1029/2018JC014102.

Craik, A. D. D., and S. Leibovich, 1976: A rational model for Langmuir circulations. *J. Fluid Mech.*, **73**, 401–426, https://doi.org/10.1017/S0022112076001420.

Etling, D., and R. A. Brown, 1993: Roll vortices in the planetary boundary layer: A review. *Bound.-Layer Meteor.*, **65**, 215–248, https://doi.org/10.1007/BF00705527.

Fairall, C. W., E. F. Bradley, J. E. Hare, A. A. Grachev, and J. B. Edson, 2003: Bulk parameterization of air-sea fluxes: Updates and verification for the COARE algorithm. *J. Climate*, **16**, 571–591, https://doi.org/10.1175/1520-0442(2003)016%3C0571:BPOASF%3E2.0.CO;2.

Forristall, G. Z., 1981: Measurements of a saturated range in ocean wave spectra. *J. Geophys. Res.*, **86**, 8075–8084, https://doi.org/10.1029/JC086iC09p08075.

Gargett, A. E., and J. R. Wells, 2007: Langmuir turbulence in shallow water: Part I. Observations. *J. Fluid Mech.*, **576**, 27–61, https://doi.org/10.1017/S0022112006004575.

——, and C. E. Grosch, 2014: Turbulence process domination under the combined forcings of wind stress, the Langmuir vortex force, and surface cooling. *J. Phys. Oceanogr.*, **44**, 44–67, https://doi.org/10.1175/JPO-D-13-021.1.

——, and D. J. Savidge, 2020: Winds, waves and turbulence on a shallow continental shelf during passage of a tropical storm.

J. Phys. Oceanogr., **50**, 1341–134, https://doi.org/10.1175/JPO-D-20-0024.1.

——, J. R. Wells, A. E. Tejada-Martínez, and C. E. Grosch, 2004: Langmuir supercells: A mechanism for sediment resuspension and transport in shallow seas. *Science*, **306**, 1925–1928, https://doi.org/10.1126/science.1100849.

Grant, A. L., and S. E. Belcher, 2009: Characteristics of Langmuir turbulence in the ocean mixed layer. *J. Phys. Oceanogr.*, **39**, 1871–1887, https://doi.org/10.1175/2009JPO4119.1.

Grosch, C. E., and A. E. Gargett, 2016: Why do LES of Langmuir supercells not include rotation? *J. Phys. Oceanogr.*, **46**, 3595–3597, https://doi.org/10.1175/JPO-D-16-0092.1.

Harcourt, R. R., and E. A. D'Asaro, 2008: Large-eddy simulation of Langmuir turbulence in pure wind seas. *J. Phys. Oceanogr.*, **38**, 1542–1562, https://doi.org/10.1175/2007JPO3842.1.

Kenyon, K. E., 1969: Stokes drift for random gravity waves. *J. Geophys. Res.*, **74**, 6991–6994, https://doi.org/10.1029/JC074i028p06991.

Leibovich, S., 1977: Convective instability of stably stratified water in the ocean. *J. Fluid Mech.*, **82**, 561–581, https://doi.org/10.1017/S0022112077000846.

Li, M., C. Garrett, and E. Skyllingstad, 2004: A regime diagram for classifying turbulent eddies in the upper ocean. *Deep-Sea Res. I*, **52**, 259–278, https://doi.org/10.1016/j.dsr.2004.09.004.

McWilliams, J. C., P. P. Sullivan, and C.-H. Moeng, 1997: Langmuir turbulence in the ocean. *J. Fluid Mech.*, **334**, 1–30, https://doi.org/10.1017/S0022112096004375.

Min, H. S., and Y. Noh, 2004: Influence of the surface heating on Langmuir circulation. *J. Phys. Oceanogr.*, **34**, 2630–2641, https://doi.org/10.1175/JPOJPO-2654.1.

Phillips, O. M., 1958: The equilibrium range in the spectrum of wind-generated waves. *J. Fluid Mech.*, **4**, 426–434, https://doi.org/10.1017/S0022112058000550.

Resio, D. T., C. E. Long, and C. L. Vincent, 2004: The equilibrium-range constant in wind-generated wave spectra. *J. Geophys. Res.*, **109**, CO1018, https://doi.org/10.1029/2003JC001788.

Romero, L., and W. K. Melville, 2010: Numerical modeling of fetch-limited waves in the Gulf of Tehuantepec. *J. Phys. Oceanogr.*, **40**, 466–486, https://doi.org/10.1175/2009JPO4128.1.

Skyllingstad, E. D., 2000: Scales of Langmuir circulation generated using a large-eddy simulation model. *Spill Sci. Technol. Bull.*, **6**, 239–246, https://doi.org/10.1016/S1353-2561(01)00042-1.

Smith, J. A., 1996: Observations of Langmuir circulation, waves, and the mixed layer. *The Air-Sea Interface: Radio and Acoustic Sensing, Turbulence, and Wave Dynamics*, M. A. Donelan, W. Hui and W. J. Plant, Eds., University of Toronto Press, 613–622.

Toba, Y., 1973: Local balance in the air-sea boundary process. *J. Oceanogr. Soc. Japan*, **29**, 209–220, https://doi.org/10.1007/BF02108528.

Walker, R., A. E. Tejada-Martínez, and C. E. Grosch, 2016: Large-eddy simulation of a coastal ocean under the combined effect of surface heat fluxes and full-depth Langmuir circulation. *J. Phys. Oceanogr.*, **42**, 2411–2436, https://doi.org/10.1175/JPO-D-15-0168.1.

Yoshikawa, Y., Y. Baba, H. Mizutani, T. Kubo, and C. Shimoda, 2018: Observed features of Langmuir turbulence forced by misaligned wind and waves under destabilizing buoyancy force. *J. Phys. Oceanogr.*, **48**, 2737–2759, https://doi.org/10.1175/JPO-D-18-0038.1.